Chapter 8

Experimental Reconstruction Results

The inverse model was tested using experimental data from scattering phantoms. We recorded measurements on three different phantoms and reconstructed cross-sectional images of the scattering and absorption coefficients. First, we tested the inverse model on a simple phantom that contained two regions with different scattering coefficients. Then, we focused our attention on scattering media that contained void-like regions. Void-containing media are encountered in several important applications, such as brain and joint imaging. The widely applied diffusion theory fails to describe light propagation in void-like areas and the ERT needs to be employed.

8.1 Phantom with Single Scattering Heterogeneity

We begin with an example that was already used in Section 6.6 on page 104 for the gradient calculation from experimental data. Now we demonstrate how the cross-sectional image of the scattering coefficient evolves throughout the optimization process by using that

gradient $\nabla_\mu \Phi$. The phantom contained a region that had a different scattering coefficient than the bulk medium. A schematic of the phantom is shown in Figure 6.7 on page 103. It contained a hole with a diameter of 0.5 cm that was filled with a diluted solution of INTRALIPID®. The optical parameters of the INTRALIPID® solution were $\mu_s' = 23.2 \pm 5$ cm^{-1} and $\mu_a = 0.00675 \pm 0.03$ cm^{-1}. The background material had the optical parameters $\mu_s = 50$ cm^{-1}, $\mu_a = 0.45$ cm^{-1}, and $g = 0.86$. The experimental data were obtained for 12×28 source-detector pairs.

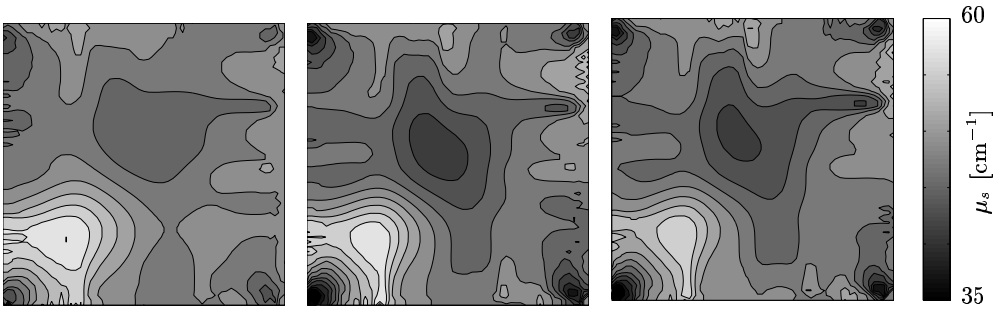

(a) After 5 iterations ($\log_{10}(\tilde{\varphi}) = -3.22$).

(b) After 8 iterations ($\log_{10}(\tilde{\varphi}) = -3.4$).

(c) After 13 iterations ($\log_{10}(\tilde{\varphi}) = -3.44$).

Figure 8.1: Reconstructed scattering coefficient μ_s after 5, 8, and 13 iterations. The region with an elevated scattering coefficient is clearly seen in the lower left corner of the images. The initial guess of the reconstruction was $\mu_{s_0} = 50$ cm^{-1}. Adjacent isolines are separated by $\mu_s = 2$ cm^{-1}.

We reconstructed the scattering coefficient μ_s using the BFGS method. The initial guess consisted of a homogeneous distribution of $\mu_{s_0} = 50$ cm^{-1}. The absorption coefficient $\mu_{a_0} = 0.45$ cm^{-1} and the anisotropy factor $g = 0.86$ were unchanged throughout the reconstruction. The forward calculations for the evaluation of the objective function were performed on a 61×61 grid with 16 ordinates. The reconstruction process was terminated after the relative difference $|(\Phi_{k+1} - \Phi_k)/\Phi_k|$ of the objective function of two subsequent

iteration steps was smaller than $\epsilon = 10^{-2}$, which yielded a total of 40 basic operations [1] (27 forward calculations + 13 gradient calculations). The reconstructed images are shown in Figure 8.1 after 5, 8, and 13 iterations. The scattering coefficient is displayed on a scale from $\mu_s = 35$ cm^{-1} to $\mu_s = 60$ cm^{-1}. Adjacent isolines in the images are separated by $\mu_s = 2$ cm^{-1}.

The scattering heterogeneity is clearly visible in the lower left corner of all three images. The heterogeneity in the reconstructed image approaches its actual size of 0.5 cm in diameter at the last iteration step. The largest scattering coefficient of the heterogeneity is $\mu_s = 59$ cm^{-1}, which results in a μ_s' of 8.26 cm^{-1} assuming $g = 0.86$. That is 18% higher than the surrounding scattering region but still smaller than the assumed reduced scattering coefficient $\mu_s' = 23.2$ cm^{-1} of the INTRALIPID® solution. This can be attributed to several facts. First, the actual optical parameters of INTRALIPID® are not exactly known (see also Section 4.3 on page 60) during the preparation of the phantom. Second, the absorption coefficient of the initial guess $\mu_{a_0} = 0.45$ cm^{-1}, which was held constant throughout the reconstruction process, and the absorption coefficient $\mu_a = 0.00675$ cm^{-1} of the diluted INTRALIPID® of the phantom did not match. Consequently, the large absorption coefficient dominantly biased the light propagation at the position of the heterogeneity and led to an underestimation of μ_s in the reconstructed image.

8.2 Phantoms with Void Regions

We reconstructed the scattering and absorption coefficients of two different phantoms to study the influence of void regions on the reconstruction results. These void regions are typically encountered in OT when images of finger joints or of the human brain are reconstructed. The first phantom had dimensions of 3 cm × 3 cm × 14 cm. It contained

[1] See definition on page 109.

three cylindrical holes with diameter of 0.5 cm each (see Figure 8.2(a)). The holes were filled with clear water. The optical parameters of the bulk material of the phantom were $\mu_s = 58 \pm 5$ cm^{-1}, $\mu_a = 0.35 \pm 0.1$ cm^{-1}, $g = 0.85$, and $n = 1.56$. A second phantom had

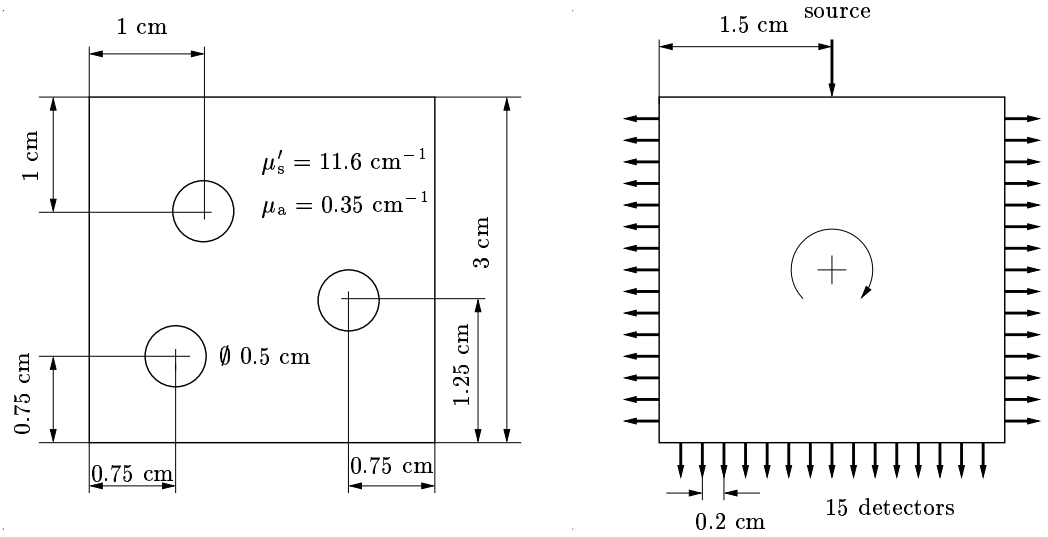

(a) Schematic of the phantom.

(b) Source-detector configuration of the phantom.

Figure 8.2: Schematic and source-detector configuration of phantom with three void-like heterogeneities. The phantom was illuminated by one source at each side.

dimensions of 4 cm × 4 cm × 14 cm and contained a void ring filled with clear water. It is similar to the phantom with a void ring in Chapter 4.2.2, but now the inner diameter of the ring is enlarged to 2.4 cm and has a thickness of 0.3 cm (see Figure 8.3(a)). The optical parameters of the background are $\mu_s = 58 \pm 1.5$ cm^{-1}, $\mu_a = 0.35 \pm 0.1$ cm^{-1}, $g = 0.8$, and $n = 1.56$. This phantom consisting of a void ring that encloses a highly scattering area is of particular interest in OT of the brain, where the clear CSF layer encloses the highly scattering white and gray matter.

Both phantoms were illuminated with near-infrared light and the outgoing light

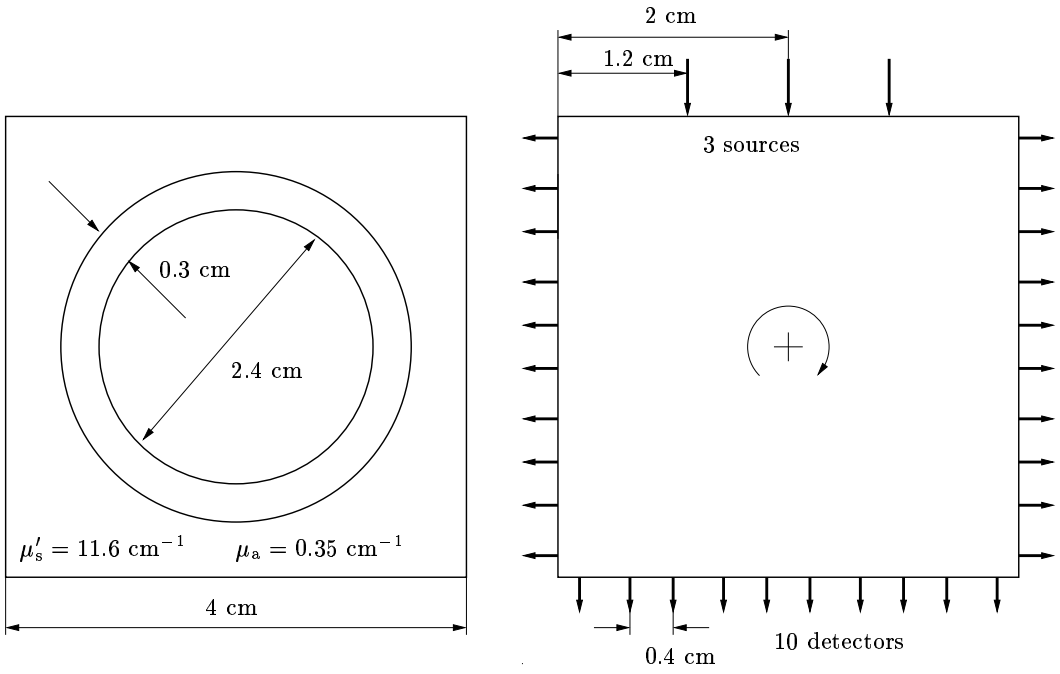

(a) Schematic of the phantom.

(b) Source-detector configuration of the phantom.

Figure 8.3: Schematic and source-detector configuration of phantom with a void-like ring. The phantom was illuminated by three sources at each side.

was measured on the phantom boundaries as explained in Chapter 4.1. The outgoing light was measured on each side (except source side) of the small phantom at 15 different detector positions with a separation of 0.2 cm [2]. The sources were located in the center of all 4 sides yielding 4×45 measurement points, see Figure 8.2(b). For the large phantom we used more source-detector points. Three sources were symmetrically placed, one on each side of the central source with a separation of 0.8 cm. 10 detector points with a separation of 0.4 cm were placed on each of the three sides (except the source) for all 12 different source positions yielding 12×30 measurement points, see Figure 8.3(b).

[2] The measurement data were supplied by Uwe Netz at the Institut für Medizinische Physik/Lasermedizin, Freie Universität Berlin.

The experimental data were supplied as input to the MOBIIR scheme, which calculated cross-sectional images of the distribution of the scattering and absorption coefficients in a horizontal plane of the phantoms. We either used the BFGS method or the CG method for finding the minimum of the objective function. The reconstruction process was completed after the relative difference $|(\Phi_{k+1} - \Phi_k)/\Phi_k|$ of the objective function of subsequent iterations was less than $\epsilon = 10^{-2}$.

The reconstructions of the phantom that contained three perturbations were done on a 61×61 grid with a grid point separation of 0.05 cm. 16 ordinates were used for the angular discretization. We started the reconstruction from an initial guess $\mu_{s_0} = 50$ cm^{-1} and $\mu_{a_0} = 0.62$ cm^{-1}. The anisotropy factor was $g = 0.85$ throughout the reconstruction. The BFGS method needed a total of 34 basic operations (18 forward and 16 gradient calculations). The reconstruction results for μ_s and μ_a are shown in Figure 8.4. Adjacent isolines are separated by $\mu_s = 4$ cm^{-1} and $\mu_a = 0.04$ cm^{-1}, respectively.

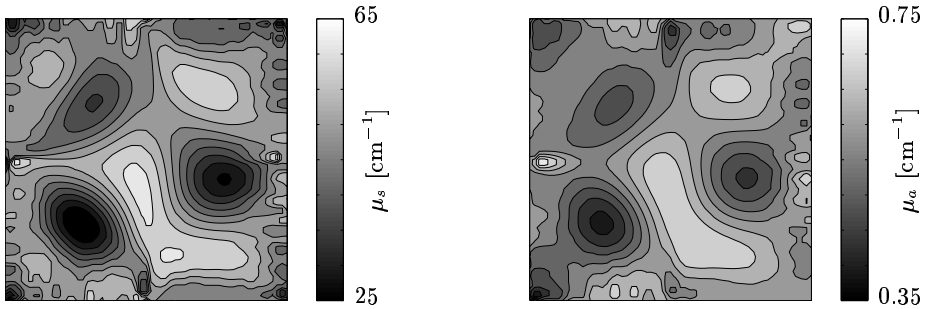

(a) Reconstructed image of the scattering coefficient μ_s.

(b) Reconstructed image of the absorption coefficient μ_a.

Figure 8.4: Reconstruction results of the phantom with three water-filled holes after 34 basic operations by using the BFGS method. Distance between adjacent isolines is $\mu_s = 4$ cm^{-1} and $\mu_a = 0.04$ cm^{-1}.

The locations of all three water perturbations are clearly reconstructed. The lo-

cation of the smallest scattering coefficient of all perturbations deviates by less than 0.1 cm from the exact center of the hole. The circular shape of the perturbations is slightly distorted in both reconstructions. The perturbation in the lower left corner, which is closest to the boundary, is reconstructed more accurately than the other two perturbations. As expected, we find that areas closer to the boundary, where the sources and detectors are located, are very sensitive to changes in the optical parameters whereas changes in the center of the phantom contribute less to the objective function. Therefore, perturbations close to the boundary are reconstructed with a higher accuracy than perturbations closer to the center of the phantom. Finally, we observe the smallest reconstructed scattering coefficient of the void areas in the image is $\mu_\mathrm{s} = 26\ \mathrm{cm}^{-1}$ and the smallest absorption coefficient is $\mu_\mathrm{a} = 0.42\ \mathrm{cm}^{-1}$. Compared to the initial guesses this equals relative changes of 48% for μ_s and 32% for μ_a.

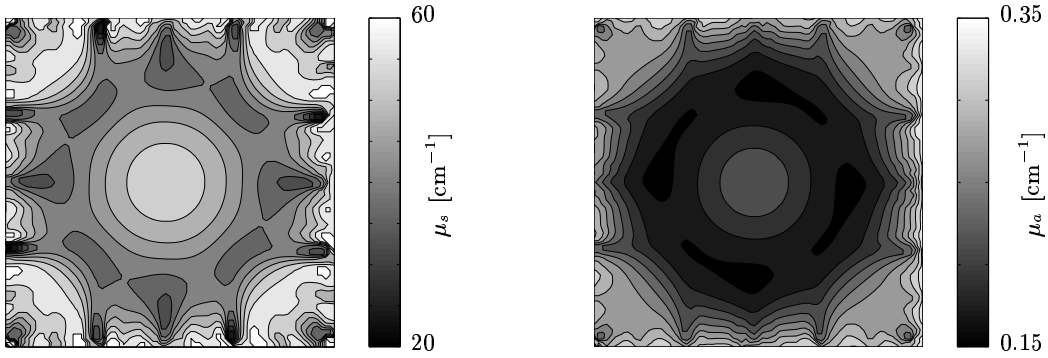

(a) Reconstructed image of the scattering coefficient μ_s.

(b) Reconstructed image of the absorption coefficient μ_a.

Figure 8.5: Reconstruction results of the phantom with a water-filled ring after 150 basic operations by using the CG method. Distance between adjacent isolines is $\mu_\mathrm{s} = 4\ \mathrm{cm}^{-1}$ and $\mu_\mathrm{a} = 0.02\ \mathrm{cm}^{-1}$.

The reconstruction of the phantom that contained a void-like ring was done on a

81×81 grid with a grid point separation of 0.05 cm. For the angular discretization we chose 16 ordinates. We started from an initial guess $\mu_{s_0} = 58$ cm^{-1} and $\mu_{a_0} = 0.35$ cm^{-1}. The anisotropy factor $g = 0.8$ was constant throughout the reconstruction. The optimization process, using the CG method, was terminated after 150 basic operations (143 forward and 7 gradient calculations). We did not use the BFGS method as in the previous example because of the huge memory requirement for the storage of the inverse Hessian $\mathcal{H}_k$. Figure 8.5 shows the reconstruction results for μ_s and μ_a. Adjacent isolines are separated by a $\mu_s = 4$ cm^{-1} and a $\mu_a = 0.02$ cm^{-1}. It can be seen that the ring structure was found in both reconstructions. The absolute values within the ring zone only decrease from the initial guesses of $\mu_{s_0} = 58$ cm^{-1} to $\mu_s = 40$ cm^{-1}, and $\mu_{a_0} = 0.35$ cm^{-1} to $\mu_a = 0.16$ cm^{-1}. That equals only a relative change from the initial guesses of 31% for μ_s and 54% for μ_a. However, the width of the ring appears broadened, especially in the μ_a-image.

8.3 Discussion

In both cases, void-like ring and three void-like cylinders in a homogeneous background, we find that while the position of the voids are accurately determined, the absolute values of the optical parameters within the voids are underestimated. This is most likely caused by the fact that the initial guess is very far away from the true value in these areas. It is well known that OT is an ill-posed problem and that different distributions of optical parameters can yield similarly small values of the objective function. For example, in the case of the void-like ring, smaller changes in the optical parameters in a broader region yield almost the same objective function as a stronger change in optical parameters in a smaller area. This problem can possibly be overcome by using different data types as shown by Schweiger and Arridge [Schweiger97] [Schweiger99].

We find that the scattering images show larger artifacts than the absorption images. For example in the case of the void-like ring (see Figure 8.5), we can see streaks of low scattering that seem to originate from the sources. The reasons for this behavior are currently unclear, but may be explained by the particular use of the upwind-difference discrete-ordinates method and highly anisotropic sources. Other groups that employ discrete-ordinates methods have observed similar *ray effects*, especially in void-like areas that are close to a source [Lathrop68] [Ackroyd86].